Theoretical Study of a W-Band-Covering Frequency Tunable Gyrotron

Fan-Hong Li, Chao-Hai Du, *Senior Member, IEEE*, Zi-Chao Gao, Shi Pan, Liang Zhang
Pu-Kun Liu, *Senior Member, IEEE*, K. Ronald, and Adrian W. Cross, *Senior Member, IEEE*

***Abstract*—The gyrotron has already demonstrated the capability of generating high-power coherent electromagnetic (EM) radiation at high frequencies and finds application in fusion plasma heating and in magnetic resonance spectroscopy. In this paper, we propose a W-band gyrotron which uses a so-called multi-mode switching scheme to realize ultra-broadband frequency tuning capability, nearly covering about 70% of the W-band (75GHz to 110GHz) range. The tuning strategy used to suppress mode competition and stabilize gun parameters in such an open-cavity multi-mode switching gyrotron is presented. Theoretical study shows that the multi-mode switching gyrotron can generate a frequency tuning range much wider than a conventional step-tuning gyrotron or a single-mode tuning gyrotron. In addition, another technology that uses a slot-assisted circuit to select only axis-symmetrical TE operating modes is presented. Using such a circuit a tuning range of about 25 GHz in the W-band is obtainable. The proposed multi-mode switching gyrotron is a promising ultra-broadband source for millimeter-wave and terahertz-wave applications.**

***Index Terms*—Gyrotron, W-band, broadband tuning.**

I. Introduction

As a portion of the electromagnetic (EM) wave spectrum, millimeter-to-submillimeter wavelength radiation possesses many merits and play an important role in many areas [1] such as plasma fusion diagnostics [2] and dynamic nuclear polarization enhanced nuclear magnetic resonance (DNP-NMR) spectroscopy, as a result of which, millimeter-wave devices have developed rapidly in the past decade.

The development of millimeter-wave technologies depends on the EM sources which can generate high-power coherent radiation in such a high-frequency band [1]-[7]. EM sources in the millimeter waveband can be divided roughly into two classifications, i.e., electronic devices and optical devices. Though optical devices such as optically pumped lasers and quantum cascade lasers can output energy of very-high-frequency EM waves, its output power is likely at most to be the milliwatt level [5]. In the millimeter and submillimeter wave band, a type of vacuum electronic device called the gyrotron, which is based on the principle of the electron cyclotron maser (ECM), has sufficient capacity to generate high-power radiation with high efficiency [5], [8], [9]. The interaction in a gyrotron occurs mainly between an EM waveguide mode and the electron cyclotron beam. The approximate radiation frequency of the output power can be determined as follows

$$\omega \approx k_z v_z + s\Omega_e \tag{1}$$

where ω is the frequency of the EM waves inside the waveguide, k_z is the longitudinal wave number, and v_z, s and Ω_e are the electron beam velocity, the cyclotron harmonic number and the relativistic cyclotron frequency, respectively [10]. The charged particles in a gyrotrons are constrained by an external magnetic field, thus, Ω_e of electrons is determined by B_0, i.e., the strength of the external magnetic field. The relation between Ω_e and B_0 are shown as follows

$$\Omega_e = \frac{B_0 e}{\gamma m_e} \tag{2}$$

where γ is the relativistic factor, and e and m_e is the charge and rest mass of electrons.

The radiation frequency of a gyrotron can be effectively tuned by alternating the strength of the magnetic field. Based on Eq. (1) and Eq. (2), the radiation frequency and B_0 have an approximately linear correlation, which means the ECM mechanism allows the output frequency to be changed by altering the strength of the external magnetic field. Frequency-tunable gyrotrons are attractive in many research areas like magnetically confined fusion plasmas [11], DNP-NMR [3], and advanced material process, and are being studied by many scientists. The frequency-tunable gyrotron can be separated into three classes [5], [12]. The first kind is the step-tunable gyrotrons [13], [14], [15]. The step-tunable gyrotron employs a high-Q open cavity and has a broad but discrete frequency range. During the magnetic tuning, the operating modes are switched sequentially. Normally, the gyrotrons generate EM energy at the near cut-off resonant frequency of each operating mode. The gyrotron can only generate radiation power at finite and discrete frequency points in the covered-frequency range. For example, the gyrotron

This work was supported by the National Science Foundation of China under Contract 61531002, Contract 61861130367, and Contract NSAF U1830201. This work was also supported in part by Newton Advanced Fellowship NAF\R1\180121 from Royal Society, United Kingdom.

F. H. Li, C. H. Du, Z. C. Gao, S. Pan and P. K. Liu are with the department of electronics, Peking University, Beijing 100871, China (e-mail: duchaohai@pku.edu.cn).

A. W. Cross, K. Ronald and L. Zhang are with the Department of Physics, SUPA, University of Strathclyde, Glasgow G4 0NG, United Kingdom.

series named Gyrotron FU Series developed by Fukui University for plasma diagnostic experiments, in Japan, can generate radiation in the range between 38 GHz to 889 GHz [15]. The second is the continuously frequency-tunable single-mode gyrotron [16], [17]. The gyrotron was designed to operate at one carefully chosen transverse mode, but more exactly, at a series of different axial modes of a specific operating mode. Different from the step-tunable gyrotron, such gyrotrons can be tuned continuously during the tuning process via continuous axial-mode transition. It can generate EM radiation in the whole tuning bandwidth rather than many discrete frequency points. However, due to the quantitatively high-Q property of fundamental axial mode in the interaction circuit, the tunable range is still relatively limited, and, especially, the interaction efficiency of higher-order axial modes drops drastically from that of the fundamental one. A gyrotron oscillator at 460 GHz with a total Q of 12000 and 1-GHz smooth frequency tuning range of the fundamental axial mode was investigated experimentally and theoretically by MIT in the USA [18].

There is a third kind of frequency-tunable gyrotron which uses the backward wave interaction [19]-[21]. With the advantages of the former two kinds of gyrotrons, the backward-wave gyrotron becomes a superior device that balances well between the covered-frequency range and ability to be continuously tuned by adjusting the cavity magnetic field [10], [19]-[27]. In order to further strengthen the performance of backward-wave interaction, a low-Q pre-bunched cavity structure is adopted [5], [10], [12]. The gyrotron can be operated at high-order axial modes. To realize a broad frequency covering range, the operating modes even can be switched sequentially during the tuning process, and such multiple operating modes are employed to combine an extraordinarily broad frequency tuning range. This paper will address the challenges using the abovementioned technology to realize a gyrotron with a frequency tuning range covering most of the W band. Such a broadband gyrotron will be a fresh-new high-power source with the capability of single source radiation production for multi-frequency high-power millimetre-wave systems.

This paper is organized as follows. Section II introduces the analysis and design of the gyro-oscillator based on the frequency-domain and time-domain theory. To verify the design, Section III introduces the analysis of the mode competition based on the calculation of coupling impedance and start-oscillation current. Section IV discusses the robustness of the electron gun and the feasibility of circular-electric-mode switching. The conclusion is finally drawn in Section V.

II. Gyrotron Design

A. Interaction Circuit Design

A pre-bunched cavity [5] is employed for this tunable gyrotron. The interaction circuit can be divided into four segments, i.e. the cut-off section, the pre-bunched cavity, the main interaction cavity and the downstream taper. The longitudinal profile of the gyrotron cavity is shown in Fig. 1. Every segment of the structure has a unique function.

Firstly, the cut-off section can decrease the energy leakage and control the reflection in the upstream taper. The cut-off section is 5 mm in length. The up-tapering inclination angle is about 19°. Because of the reflection caused by the cut-off section, this section can prevent EM energy from leaking into the electron gun area and exciting spurious oscillation in the gun tunnel. To suppress the leaking energy as much as possible, attenuation materials [8], [10] should be employed in the magnetic compression tunnel in front of the cavity.

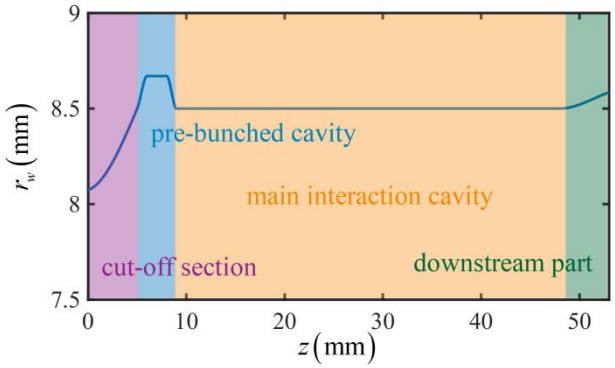

Fig. 1 The blue solid curve is the longitudinal profile of the cavity of the tunable gyrotron. The blue and red arrows indicate the propagation directions of the backward and forward wave, respectively.

Secondly, the pre-bunching cavity at the upstream end is employed to enhance the efficiency of the backward-wave interaction and broaden the covered-frequency range, indirectly. The geometric profile of the cavity in the longitudinal section is an isosceles trapezoid. The radius of the pre-bunched section is extended by 0.17 mm. The pre-bunching cavity is short enough to suppress local spurious oscillation. Normally, the electrons injected from the upstream side are firstly modulated by the EM waves in this section. During this process, the electrons slightly gains energy and experience forced detuning of the bunching. After that, the bunched electrons will interact with the EM waves in the following section. This part of the interaction circuit can enhance the modulation effect of the electron beam imposed by the backward wave. The losing-energy length of the interaction will be reduced by half as compared to the bunching length in a conventional single-uniform-section open cavity. As a result, the electrons in the pre-bunching interaction cavity will enter the state of being able to release energy faster than that in the classical open-cavity circuit [5].

Thirdly, the main cavity is the space where electrons interact with the backward component of the EM wave. The length of the main part has an apparent influence on the efficiency of the beam-wave interaction. The main cavity is a uniform cylindrical waveguide with a length of 39 mm and a radius of 8.5 mm. In the backward wave interaction area, the efficiency of the beam-wave interaction is not as high as that in the near cut-off area. To enhance efficiency, the length of the main interaction cavity is extended under the principle of single-mode operation. However, this length extension also needs to consider another two problems, namely, ohmic loss and non-stationary oscillation. The ohmic loss, as well as the

thermal effect, usually originates from the finite electrical conductivity and the surface current on the cavity wall. Usually, the waveguide is made of oxygen-free copper to reduce ohmic loss. Non-stationary oscillation has been studied by many scientists before [28], [29], The reflection from one of the cavity ends is important in controlling the stationary zone [29]. In other words, another function of the cut-off section is to alter the phase of the reflected wave in the upstream section.

Lastly, the downstream section functions as a junction between the interaction circuit and the output taper. The length included in the simulation is 5 mm, and the inclination angle is 1.0°. Because of the reflection from the upstream and downstream tapers, the cavity is similar to an open cavity. This kind of structure has the advantage of being continuously tunable and supporting efficient backward-wave interaction. That is the main reason why we use such a pre-bunched structure.

B. Mode Selection

The operating modes selected here are high-radial-index modes (HRIM), and the EM energy of the modes us located mostly near the axis of the cylindrical waveguide.

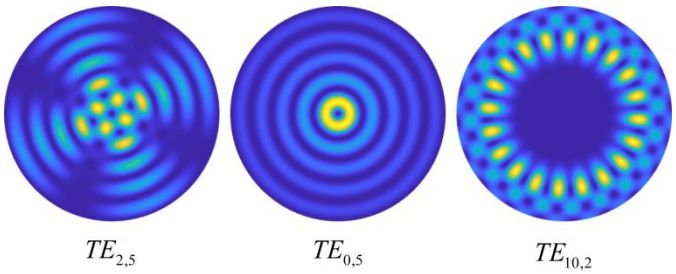

Fig. 2. The transverse-field distribution of the modes $TE_{2,5}$, $TE_{0,5}$ and $TE_{10,2}$. The eigenvalues of these modes are 16.35, 16.47 and 16.45, respectively.

The differences in the electric field between HRIMs and low-radial-index modes (LRIM) can be distinguished through some examples in Fig. 2. HRIMs have some apparent advantages. Firstly, due to the distribution in the cross-section, the surface currents of these modes under the same power are lower than those of the LRIMs. Thus, the ohmic loss will be smaller as well. In the cylindrical waveguide, the power can be derived as follow,

$$\begin{aligned} P &= \frac{1}{2}\mathrm{Re}\left[\int_0^a\int_0^{2\pi} E\times H^*\cdot d\vec{S}\right] \\ &= A^2\frac{\omega\mu_0 k_z}{k_\perp^2}\cdot\pi r_w^2\left(1-\frac{m^2}{x_{mn}^2}\right)J_m^2\left(x_{mn}\right) \end{aligned} \tag{3}$$

where A is an undetermined coefficient, μ_0 is the vacuum permeability, m is the azimuthal index, and k_z and $k_\perp$ are the longitudinal and transverse wavenumber, respectively. The surface current satisfied the following equation,

$$\begin{aligned} \vec{J} &= \hat{\rho}\times\vec{H} \\ &= \left[-AJ_m\left(k_\perp r_w\right)e^{j(\omega t-m\phi-k_z z)}\right]\hat{\phi} \\ &+\left[-A\frac{mk_z}{k_\perp^2 r_w}J_m\left(k_\perp r_w\right)e^{j(\omega t-m\phi-k_z z)}\right]\hat{z} \end{aligned} \tag{4}$$

If the input power of every TE mode is set as the same value, A can be calculated. Thus, the surface current of every TE mode under the same power can be calculated. For better comparison, the surface currents of the TE mode demonstrated in Fig. 2 are calculated and shown in Fig. 3.

Secondly, the annular hollow electron beam injected into the waveguide usually locates at the peak electric field region. When the operating modes are LAIMs, the guiding center radiuses of the electron beams will be large. Different from LAIMs, the maximums of the electric fields of HAIMs usually locate near the axis of the cylindrical waveguide, as a result of which, the electron beams interacting with operating modes stay far away from the wall of the waveguides. Electrons are not likely to hit the wall. We decided to use the modes $TE_{0,4}$, $TE_{2,5}$, $TE_{1,5}$ and $TE_{1,6}$ as the operating modes as a balance between the ohmic loss and the problem of mode competition.

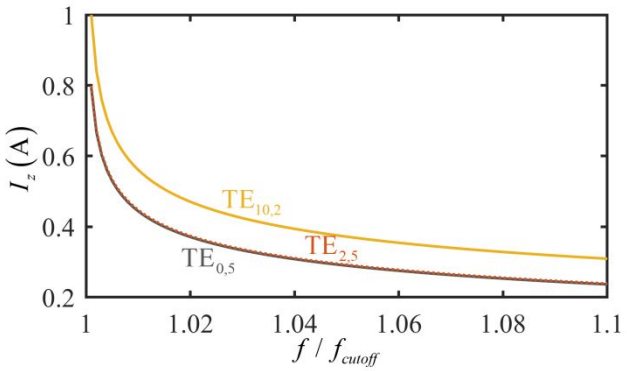

Fig. 3. The surface current of the TE0,5, TE2,5 and TE10,2 mode. The power of the three modes is set as the same value.

For a cylindrical waveguide, the cut-off frequency of every TE mode can be determined by

$$f = \frac{c\cdot x_{m,n}}{2\pi r_w} \tag{5}$$

while c is light speed in a vacuum, $x_{m,n}$ is the eigenvalue, i.e., the n^{th} root of the derivative of the m-order first kind Bessel function, and r_w is the radius of the main interaction cavity. The inner radius of the main interaction circuit can be derived by using (3). The essential parameters are detailed in Tab. I. The cut-off frequencies of the four operating modes $TE_{0,4}$, $TE_{1,5}$, $TE_{2,5}$ and $TE_{1,6}$ are 74.79 GHz, 83.43 GHz, 91.76 GHz, 101.13 GHz, respectively. We use a low voltage of 5 kV as the working voltage. Low voltage gyrotrons have a broader tuning range than high voltage gyrotrons.

TABLE I
OPERATING PARAMETERS OF THE GYRO-OSCILLATOR.

Operating parameters	Value
Operating modes	$TE_{0,4}$, $TE_{1,5}$, $TE_{2,5}$, $TE_{1,6}$

Radius	r_w = 8.5 mm
Longitudinal length	53 mm
Harmonic number	1
External magnetic field	2.63 - 3.92T
Covered-frequency range	25.12 GHz (71.78%)
Voltage	5 kV
Current	0.5 A
Pitch factor	1.5
Velocity spread	7 %
Guiding center radius	r_g = 824.5 μm

Dynamic simulations of beam-wave interaction during magnetic-field tuning in the cavity were carried out using the time-domain program [26], [28]-[32], and results are shown in Fig. 3 (a). The power carried by the electron beam is 2.5 kW. The peak interaction efficiencies of the $TE_{0,4}$ mode, the $TE_{1,5}$ mode, the $TE_{2,5}$ mode and the $TE_{1,6}$ mode are 20.2%, 20.1 %, 17.4% and 21.3%, respectively. The frequency spectra of the interaction modes are demonstrated in Fig. 3 (b). The spectra are derived by using the fast Fourier transform algorithm. The frequency ranges covered by the $TE_{0,4}$ mode, the $TE_{1,5}$ mode, the $TE_{2,5}$ mode and the $TE_{1,6}$ mode are 5.68 GHz, 6.91 GHz, 7.86 GHz, and 4.69 GHz, respectively. The total covered-frequency range is 25.14 GHz, which covered about 71% of the whole W-band range. The frequency gaps that are not covered can be seen in Fig. 3 (b). It is a result of the velocity spread of the electron beam and the mode switching. Due to the velocity spread of the electron gun, the interaction efficiency decreases in the area far away from the cut-off frequency. Though the interaction efficiency can be enhanced, it's also insurmountable for a waveguide mode to cover a very large frequency range because of the mode switching in the backward-wave region.

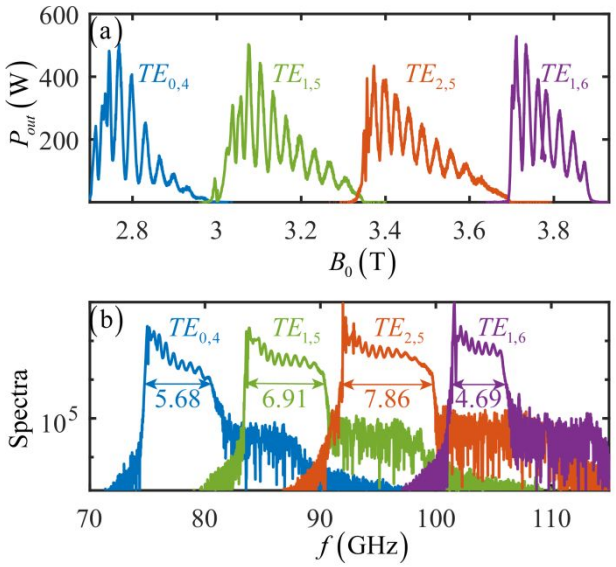

Fig. 3 (a) Output power calculated by using multi-mode time-domain program. (b) Frequency spectra calculated by using the fast Fourier transform algorithm. The colored number is the covered-frequency range of every mode, and the unit is GHz. The total covered-frequency range is 25.14 GHz, which covers more than 70% of the whole W-band range.

III. Mode Competition Analysis

According to Eq. (3) and the parameters in Tab. I, the cut-off frequency of every TE mode can be derived, which can be used to find out the competition modes. The desired frequency range is from 75 GHz to 110 GHz. To ensure the feasibility of this design, the frequency range used to find out the competition modes is chosen from 65 GHz and 120 GHz, which means the $x_{m,n}$ is from 11.57 to 21.38. Based on the cold dispersion relations, the competing modes can be roughly determined. The dispersion plot is composed of two parts. One is the hyperbola which corresponds to the TE mode. The TE mode line is only one branch of the hyperbola. Another is a straight line which corresponds to the electron beam. The ordinate values of the intersections between the hyperbolas and the coordinate axis are equal to their own cut-off frequencies. We calculate the beam-wave coupling factor H_{sm} [33] of all the modes plotted in Fig. 4 (a) and the ones with highest possibility to oscillate are shown in Fig. 4 (b). However, lots of H_{sm} of the TE modes are quantitively small. As a result, not all H_{sm} curves can be observed. The competition modes for every operating mode are different. Firstly, the competition modes around the $TE_{0,4}$ mode are the $TE_{1,4}$ mode and the $TE_{2,4}$ mode.

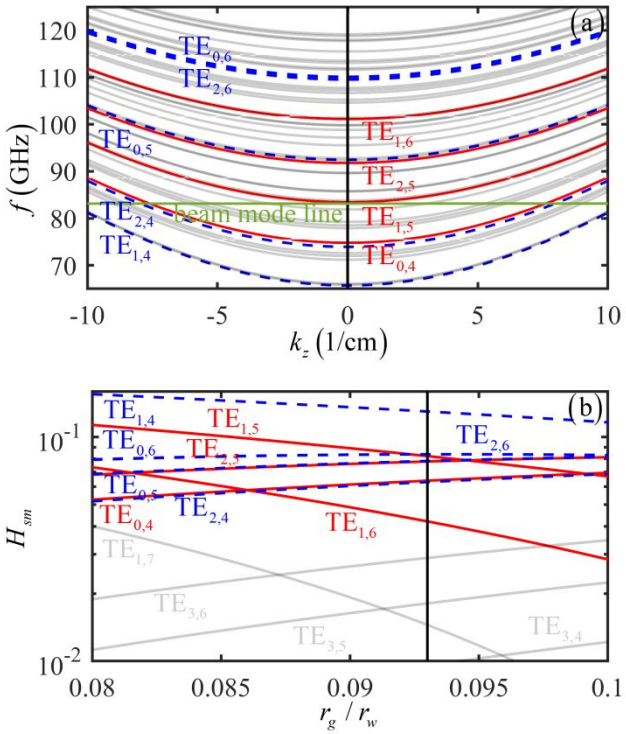

Fig. 4 (a) Cold dispersion diagram of operating modes and competition modes. The green straight line is the beam mode line. The hyperbolas indicate the waveguide modes. The red solid curves indicate the operating modes. The blue dashed curves indicate the competition modes. The gray solid lines are other TE modes in the W-band range. (b) Beam-wave coupling factors versus the ratio of r_g to r_w. The black straight line shows the adopted value of r_g. The red solid curves indicate the operating modes, and the blue dashed curves indicate the competition modes. The gray solid line is the $TE_{3,6}$ mode. Since the coupling factors are quantitively small values, the H_{sm} curves of other modes are not shown.

may cause problems without a proper setup of the interaction circuit. Both the cut-off frequency and the coupling factor are

very close. Secondly, the competition modes around the $TE_{1,5}$ mode is $TE_{3,4}$. During the mode switching, the competition modes are the $TE_{0,4}$ mode and the $TE_{0,5}$ mode. Thirdly, the competition mode around the $TE_{2,5}$ mode is mainly the $TE_{0,5}$ mode. Lastly, like the $TE_{1,5}$ mode, the competition mode around the $TE_{1,6}$ mode is $TE_{3,5}$ according to H_{sm}. And the mode competition also happens during the mode switching. To better analyze the modes competition, the start-oscillation currents of the modes mentioned above were calculated using the frequency-domain program [8], [32], [34], and the calculation results are detailed in Fig. 5. As shown in Fig. 5, the curves of the $TE_{0,n}$ modes and the $TE_{2,n}$ modes are very close. The different abscissa of the minimum of every mode inspires us with a good method to suppress the mode competition.

Firstly, to suppress the $TE_{1,4}$ mode and the $TE_{2,4}$ mode, we can set the initial value of the external magnetic field at 2.698 T, thus, $TE_{0,4}$ mode here has a lower start-oscillation current than those of the $TE_{1,4}$ mode and the $TE_{2,4}$ mode. According to the previous study, the mode with the lowest start-oscillation current tends to be the dominant modes and suppresses others [5], [30], [35]. Therefore, the $TE_{0,4}$ mode can be excited and the modes $TE_{1,4}$ and $TE_{2,4}$ will be suppressed. The start-oscillation current of the $TE_{0,4}$ mode is still lower than that of the $TE_{2,4}$ mode with the magnetic field larger than 2.698 T, which means that the $TE_{0,4}$ mode interacts with the particles more strongly than the $TE_{2,4}$ mode. The $TE_{2,4}$ mode will be suppressed during the whole tuning. The related simulation results are shown in Fig. 6 (a). At 0 ns, the $TE_{0,4}$ mode and the $TE_{2,4}$ mode both start oscillation. After 20 ns, the $TE_{0,4}$ mode prevails, and the $TE_{2,4}$ mode is suppressed. The output power of the $TE_{0,4}$ mode is three order of magnitudes higher than that of the $TE_{2,4}$ mode and 10^5 times higher than those of other competition modes at the peak value, approximately.

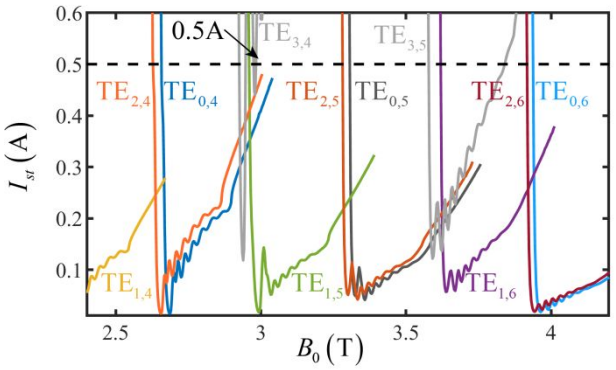

Fig. 5 Start-oscillation currents of the operating modes and the potential competition modes. The minimums of the operating-mode curves are at 2.687 T, 2.992 T, 3.359 T and 3.637 T. The black dashed line indicates the operating current produced by the MIG.

Secondly, when the magnetic field is tuned approximately to 3.0 T, the operating mode will gradually switch into the $TE_{1,5}$ mode. Mode switching can be considered as a special mode competition that a new mode will replace the old mode as the operating mode. During the process, the $TE_{0,4}$ mode will experience strong mode competition blossoming into the $TE_{1,5}$ mode. The operating frequency $TE_{0,4}$ mode is far away from its cut-off frequency, while the $TE_{1.5}$ mode is strongly coupling with the beam near the cut-off frequency. During the mode competition process, the total output power will decrease until one mode suppresses another. Although the start current of $TE_{3,4}$ mode is lower than that of the $TE_{0,4}$ mode, the $TE_{3,4}$ still cannot start oscillation. The beam modulated by the $TE_{0,4}$ mode can be seen as a beam with a large velocity spread. Thus, the start current of the $TE_{3,4}$ mode needs to be lower to start oscillation.

Thirdly, the mode competition between the $TE_{0,5}$ and $TE_{2,5}$ modes is similar to that between the modes $TE_{0,4}$ and $TE_{2,4}$. However, the start-up scenario between the $TE_{0,5}$ and $TE_{2,5}$ modes is not as strong as that between the $TE_{0,4}$ and $TE_{2,4}$ modes. The $TE_{2,5}$ mode will start oscillation first during the forward tuning. However, the start-oscillation current of the $TE_{2,5}$ mode is not always lower than that of the $TE_{0,5}$ mode as shown in Fig. 5. Since the operating current is 12 times higher than the start-oscillation current of the $TE_{0,5}$ mode at 3.359 T, the $TE_{0,5}$ can start oscillation though under the suppression of the $TE_{2,5}$ mode. However, given enough time, the $TE_{2,5}$ can gradually suppress the $TE_{0,5}$ mode as evidenced in the related simulation results shown in Fig. 6 (b). The output power of the $TE_{2,5}$ mode is 500 times higher than that of the $TE_{0,5}$ mode and 10^5 times higher than those of other competition modes at the peak operating point.

Lastly, the $TE_{1,6}$ mode is similar to the $TE_{1,5}$ mode. A 3.637 T magnetic field is a good value to make the only operating mode as mode competition induced by the $TE_{3,5}$ mode can be suppressed.

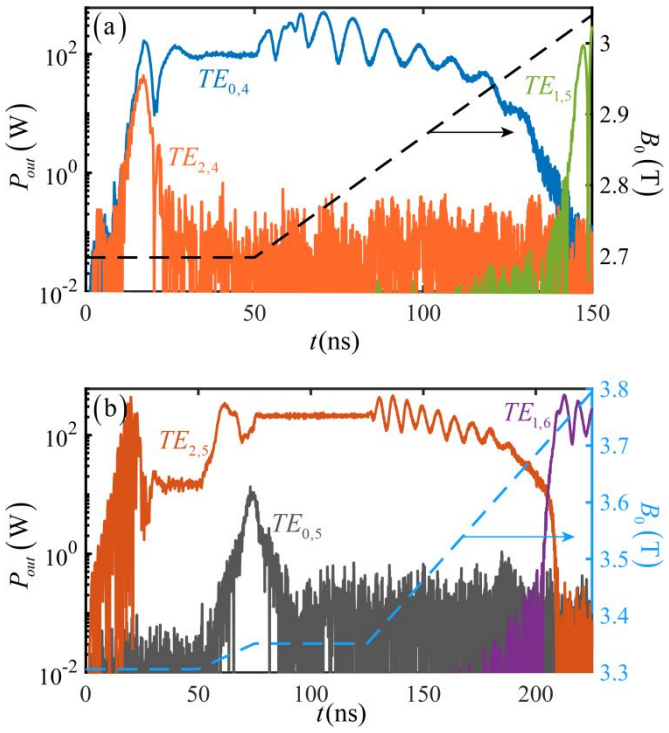

Fig. 6 Dynamic results of the operating modes and the competitive modes. (a) The solid curves indicates the output power of the modes $TE_{0,4}$, $TE_{2,4}$ and $TE_{1,5}$. The dashed curves shows the value of the external magnetic field. (b) The solid curves indicates the output power of the modes $TE_{0,5}$, $TE_{2,5}$ and $TE_{1,6}$. The dashed curve shows the value of the external magnetic field.

Moreover, the ripples in the curves above is not related to non-stationary oscillation. This can be verified from Fig. 6. In Fig. 6 (a), the output power tends to be steady in time 35 ns to 50 ns after the start-oscillation process. In Fig. 6 (b), the output power is steady in time 35 ns to 50 ns and 75 ns to 125 ns. In both Fig. 6 (a) and Fig. 6 (b), the ripples only appear during the magnetic tuning. There are no apparent period ripples in the output-power curves except when the magnetic field in being tuned. During the tuning process, the axial modes will change. The axial-mode transition is likely to be the main reason why there are ripples in the curves of the output power. When one axial mode dominates, the interaction is strong without the mode competition from other axial modes. Thus, the output power is relatively high. When at least two axial modes exist in the same waveguide, those modes will interfere with each other. This kind of axial-mode competition can lower the strength of the beam-wave interaction of each axial mode. The total output power is thus decreased. In a word, the beam-wave efficiency can reach a peak value when only one axial mode becomes the main operating mode and reaches the valley of the switching point between two axial modes.

IV. Discussion

A. Electron gun

During the tuning process, the stability of the electron gun parameters is important to the beam-wave interaction efficiency. In this paper, we propose a gyrotron design using a 5-kV, 0.5-A beam. However, the design and fabrication of an electron gun that are stable over a wide range of magnetic fields is relatively challenging, and many problems need to be overcome. The first is how to produce a 5-kV, 0.5-A beam. In the previous study, a MIG had been proposed with pitch factor α = 1.5 and velocity spread $\Delta\beta_z$ = 6% [12]. Inspired by that investigation, a magnetron injection gun (MIG) was adopted for the design in this paper. Secondly, the beam parameters cannot stay ideally constant during a long-span magnetic tuning, and the changes are likely to influence the output performance, as shown in Fig. 7 (a). During the magnetic tuning, α fluctuates a lot with the strength of the external magnetic field. An auxiliary coil can be used to make α a constant value [36]. Adjusted by the auxiliary coil, the performance of the MIG can be improved, as demonstrated in Fig. 7 (b) The velocity spread in Fig. 7 was calculated by the EGUN program [37]. Thus, only the spread caused by the MIG structure is taken into consideration. To ensure the feasibility, the velocity spread induced by the surface roughness and the thermal effect was combined with the EGUN results. The total velocity spread is nearly 7.5 %, which was adopted in the time-domain simulation.

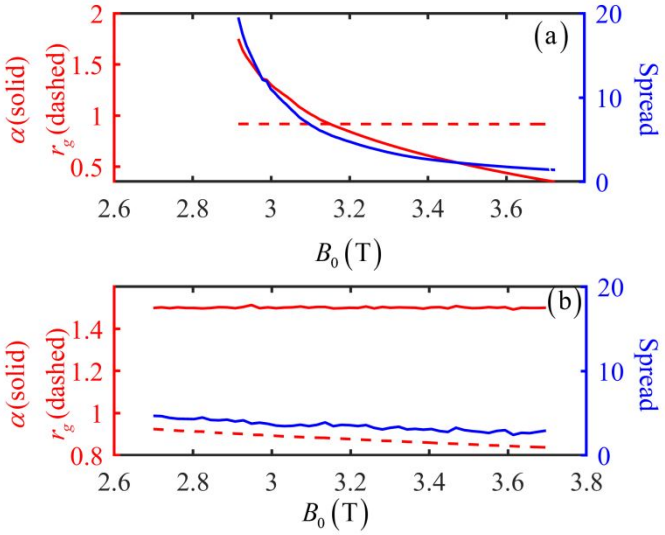

Fig. 7 (a) The performance of the MIG without the auxiliary coil. The red solid line indicates the pitch factor. The red dashed line shows the guiding center radius. And the velocity spread is demonstrated by the blue solid line. (b) The performance of the MIG with the auxiliary performance.

B. Feasibility of circular-electric-mode switching.

It is attractive to use only circular electric modes as operating modes that greatly facilitate efficient power output by using a quasi-optical mode converter. As the filtering out of non-asymmetry modes $TE_{m,n}$ ($m\neq0$) is possible using additional mode suppression techniques, we simply assume that there are only $TE_{0,n}$ modes operating, where the mode competition from non-asymmetry modes can be effectively suppressed. Without the mode competition, a higher ampere beam could be adopted to excite the operating mode. Thus, the output power of the gyrotron can be further increased. The related results of the time-domain simulation with the circular electric modes only are shown in Fig. 8. A beam current of 2 A is used. Without the $TE_{1,5}$ mode and the $TE_{1,6}$ mode, the guiding center radius is changed to 1.037 mm. As demonstrated in Fig. 8 (a), the peak interaction efficiencies of the $TE_{0,4}$ mode and the $TE_{0,5}$ mode are 11.1% and 20.7%, respectively. The frequency spectra of the interaction modes are demonstrated in Fig. 8 (b). The frequency ranges covered by the $TE_{0,4}$ mode and the $TE_{0,5}$ mode are 14.42 GHz and 13.11 GHz, respectively. The total covered-frequency range is 27.52 GHz, which is equivalent to about 79% of the whole W-band range.

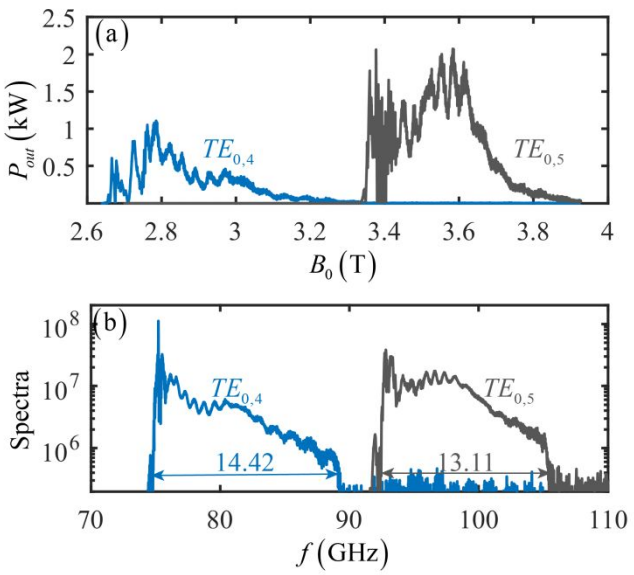

Fig. 8 (a) The output power of the $TE_{0,4}$ mode and the $TE_{0,5}$ mode. (b) The frequency spectrum of the $TE_{0,5}$ mode and $TE_{0,5}$ mode. The frequency range is 14.42 GHz and 13.11 GHz, respectively. And the total frequency range is 27.53 GHz, which is a little large than that in Fig. 3 (b).

Operation with only TE0,n modes is likely to be feasible using an azimuthally slotted-waveguide circuit. According to the previous study [22], the TE modes, except for the $TE_{0,n}$ modes, will radiate out when passing inside a waveguide with a circular slot in the azimuthal direction. A waveguide with a series of narrow slots can be employed to filter out the non-asymmetry TE modes. Usually, the width of slots is far less than the wavelength. These slots will cut off the surface currents in the z direction. The EM energy can radiate out, and the surface currents in the z direction are considered as the source of the radiation.

V. Conclusion

The paper demonstrates the design and analysis of a W-band-covering gyrotron. To realize continuously broadband tuning, we take the advantage of two classic tuning gyrotron, i.e., the discrete-frequency step-tunable gyrotron and the continuously frequency-tunable open-cavity gyrotron. The pre-bunched cavity is employed to enhance the interaction efficiency and to further broaden the frequency range. The waveguide modes of the gyrotron are high-radial-index modes $TE_{0,4}$, $TE_{1,5}$ and $TE_{2,5}$ and $TE_{1,6}$. By applying the mode switching technology, about 25 GHz frequency range is theoretically achievable, which covers more than 70% of the W-band frequency range. A special start-up scenario was introduced to establish a single-mode operating state during the tuning process, which was verified by using both a frequency-domain program and a time-domain program. In the end, we discuss some critical problems related to the electron gun and the feasibility of only circular-electric-mode switching. Such a gyrotron with the multi-mode switching technology will be promising in developing ultra-broadband sources for millimeter-wave and terahertz-wave radiation.

Reference

[1] M. Thumm, "Novel applications of millimeter and submillimeter wave gyro-devices," *J. Infrared Millim. Terahertz Waves*, vol. 22, no. 3, pp 377-386, 2001. DOI: 10.1023/A:1010799620273.

[2] M. Thumm, "MW gyrotron development for fusion plasma applications," *Plasma Phys. Control. Fusion*, vol. 45, no. 12A, 2003. DOI: 10.1088/0741-3335/45/12A/011.

[3] E. A. Nanni, A. B. Barnes, R. G. Griffin, and R. J. Temkin, "THz Dynamic Nuclear Polarization NMR," *IEEE Trans. THz Sci. Technol.*, vol. 1, no. 1, pp. 145-163, Aug. 2011. DOI: 10.1109/TTHZ.2011.2159546.

[4] K. Sassen, and Z. Wang, "Classifying clouds around the globe with the CloudSat radar: 1-year of results," *Geophys. Res. Lett.*, vol. 35, no. 4, 2008. DOI: 10.1029/2007GL032591.

[5] C. H. Du, X. B. Qi, L. B. Kong, P. K. Liu, Z. D. Li, S. X. Xu, Z. H. Geng, and L. Xiao, "Broadband Tunable Pre-Bunched Electron Cyclotron Maser for Terahertz Application," *IEEE Trans. THz Sci. Technol.*, vol. 5, no. 2, pp. 236-243, 2015. DOI: 10.1109/TTHZ.2014.2378071.

[6] D. L. Woolard, R. Brown, M. Pepper, and M. Kemp, "Terahertz frequency sensing and imaging: A time of reckoning future applications," *Proc. IEEE*, vol. 93, no. 10, pp. 1722-1743, 2005. DOI: 10.1109/JPROC.2005.853539.

[7] G. S. Nusinovich, R. Pu, T. M. Antonsen, O. V. Sinitsyn, J. Rodgers, A. Mohamed, J. Silverman, M. Al-Sheikhly, Y. S. Dimant, G. M. Milikh, M. Y. Glyavin, A. G. Luchinin, E. A. Kopelovich, and V. L. Granatstein, "Development of THz-range gyrotrons for detection of concealed radioactive materials," *J. Infrared Millim. Terahertz Waves.*, vol. 32, no. 3, pp. 380-402, 2011. DOI: 10.1007/s10762-010-9708-y.

[8] K. R. Chu, "The electron cyclotron maser," *Rev. Mod. Phys.*, vol. 76, no. 2, pp. 489-540, Apr. 2004. DOI: 10.1103/RevModPhys.76.489.

[9] J. H. Booske, R. J. Dobbs, C. D. Joye, C. L. Kory, G. R. Neil, G. S. Park, J. Park, and R. J. Temkin, "Vacuum Electronic High Power Terahertz Sources," *IEEE Trans. THz Sci. Technol.*, vol. 1, no. 1, pp. 54-75, 2011. DOI: 10.1109/TTHZ.2011.2151610.

[10] C. H. Du, X. B. Qi, P. K. Liu, T. H. Chang, S. X. Xu, Z. H. Geng, B. L. Hao, L. Xiao, G. F. Liu, Z. D. Li, S. H. Shi, and H. Wang, "Theory and Experiment of a W-Band Tunable Gyrotron Oscillator," *IEEE Trans. Electron Devices.*, vol. 61, no. 6, pp. 1781-1788, 2014. DOI: 10.1109/TED.2013.2294689.

[11] G. Dammertz, S. Alberti, A. Arnold, D. Bariou, E. Borie, P. Brand, H. Braune, V. Erckmann, G. Gantenbein, E. Giguet, R. Heidinger, J. P. Hogge, S. Illy, J. Jin, W. Kasparek, K. Koppenburg, H. P. Laqua, F. Legrand, W. Leonhardt, C. Liévin, R. Magne, G. Michel, G. Müller, G. Neffe, B. Piosczyk, T. Rzesnicki, M. Schmid, M. Thumm, M. Tran, and X. K. Yang, "Development of multimegawatt gyrotrons for fusion plasma heating and current drive," *IEEE Trans. Electron Devices.*, vol. 52, no. 5, pp. 808-817, 2005. DOI: 10.1109/TED.2005.845859.

[12] S. Pan, C. H. Du, X. B. Qi, and P. K. Liu, "Broadband terahertz-power extracting by using electron cyclotron maser," *Sci. Rep.*, vol. 7, no. 1, p. 7265, Aug 4 2017. DOI: 10.1038/s41598-017-07545-6.

[13] K. E. Kreischer, and R. J. Temkin, "Single-mode operation of a high-power, step-tunable gyrotron," *Phys. Rev. Lett.*, vol. 59, no. 5, pp. 547-550, 1987. DOI: 10.1103/PhysRevLett.59.547.

[14] M. Thumm, A. Arnold, E. Borie, O. Braz, G. Dammertz, O. Dumbrajs, K. Koppenburg, M. Kuntze, G. Michel, B. Piosczyk, "Frequency step-tunable (114–170 GHz) megawatt gyrotrons for plasma physics applications," *Fusion Eng. Des.*, vol. 53, no. 1-4, pp. 407-421, 2001, DOI: 10.1016/S0920-3796(00)00519-6

[15] T. Idehara, I. Ogawa, S. Mitsudo, M. Pereyaslavets, N. Nishida, and K. Yoshida, "Development of frequency tunable, medium power gyrotrons (Gyrotron FU series) as submillimeter wave radiation sources," *IEEE Trans. Plasma Sci.*, vol. 27, no. 2, pp. 340-354, 1999. DOI: 10.1109/27.772260.

[16] A. C. Torrezan, S. T. Han, I. Mastovsky, M. A. Shapiro, J. R. Sirigiri, R. J. Temkin, A. B. Barnes, and R. G. Griffin, "Continuous-Wave Operation of a Frequency-Tunable 460-GHz Second-Harmonic Gyrotron for Enhanced Nuclear Magnetic Resonance," *IEEE Trans. Plasma Sci.*, vol. 38, no. 6, pp. 1150-1160, Jun. 2010. DOI: 10.1109/TPS.2010.2046617.

[17] Y. Matsuki, Ke. Ueda, T. Idehara, R. Ikeda, K. Kosuga, I. Ogawa, S. Nakamura, M. Toda, T. Anai, and T. Fujiwara, "Application of Continuously Frequency-Tunable 0.4 THz Gyrotron to Dynamic Nuclear Polarization for 600 MHz Solid-State NMR," *J. Infrared Millim. Terahertz Waves.*, vol. 33, no. 7, pp. 745-755, 2012. DOI: 10.1007/s10762-012-9890-1.

[18] M. K. Hornstein, V. S. Bajaj, R. G. Griffin, K. E. Kreischer, I. Mastovsky, M. A. Shapiro, J. R. Sirigiri and R. J. Temkin, "Second harmonic operation at 460 GHz and broadband continuous frequency tuning of a gyrotron oscillator," *IEEE Trans. Electron Devices.*, vol. 52, no. 5, pp. 798-807, 2005. DOI: 10.1109/TED.2005.845818.

[19] T. H. Chang, C. T. Fan, K. F. Pao, K. R. Chu, and S. H. Chen, "Stability and tunability of the gyrotron backward-wave oscillator," *Appl. Phys. Lett.*, vol. 90, no. 19, p. 191501, 2007. DOI: 10.1063/1.2737135.

[20] C. S. Kou, "Starting oscillation conditions for gyrotron backward wave oscillators," *Phys. Plasmas.*, vol. 1, no. 9, p. 3093, 1994. DOI: 10.1063/1.870500.

[21] C. S. Kou, C. H. Chen, and T. J. Wu, "Mechanisms of efficiency enhancement by a tapered waveguide in gyrotron backward wave oscillators," *Phys. Rev. E*, vol. 57, no. 6, pp. 7162-7168, 1998. DOI: 10.1103/PhysRevE.57.7162.

[22] N. C. Chen, C. F. Yu, C. P. Yuan, and T. H. Chang, "A mode-selective circuit for TE_{01} gyrotron backward-wave oscillator with wide-tuning range," *Appl. Phys. Lett.*, vol. 94, no. 10, p. 101501, 2009. DOI: 10.1063/1.3097236.

[23] S. V. Samsonov, G. G. Denisov, V. L. Bratman, A. A. Bogdashov, M. Y. Glyavin, A. G. Luchinin, V. K. Lygin, and M. K. Thumm, "Frequency-Tunable CW Gyro-BWO With a Helically Rippled Operating Waveguide," *IEEE Trans. Plasma Sci.*, vol. 32, no. 3, pp. 884-889, 2004. DOI: 10.1109/TPS.2004.828871.

[24] W. He, C. R. Donaldson, L. Zhang, K. Ronald, P. McElhinney, and A. W. Cross, "High Power Wideband Gyrotron Backward Wave Oscillator Operating towards the Terahertz Region," *Phys. Rev. Lett.*, vol. 110, no. 16, 2013. DOI: 10.1103/PhysRevLett.110.165101.

[25] W. He, K. Ronald, A. R. Young, A. W. Cross, A. D. R. Phelps, C. G. Whyte, E. G. Rafferty, J. Thomson, C. W. Robertson, D. C. Speirs, S. V. Samsonov, V. L. Bratman, and G. G. Denisov, "Gyro-BWO Experiments Using a Helical Interaction Waveguide," *IEEE Trans. Electron Devices*, vol. 52, no. 5, pp. 839-844, 2005. DOI: 10.1109/TED.2005.845858.

[26] S. H. Kao, C. C. Chiu, P. C. Chang, K. L. Wu, and K. R. Chu, "Harmonic mode competition in a terahertz gyrotron backward-wave oscillator," *Phys. Plasmas*, vol. 19, no. 10, p. 103103, 2012. DOI: 10.1063/1.4757215.

[27] X. B. Qi, C. H. Du, and P. K. Liu, "High-Efficiency Excitation of a Third-Harmonic Gyrotron," *IEEE Trans. Electron Devices.*, vol. 62, no. 10, pp. 3399-3405, 2015. DOI: 10.1109/TED.2015.2461657.

[28] S. H. Chen, K. R. Chu, and T. H. Chang, "Saturated Behavior of the Gyrotron Backward-Wave Oscillator," *Phys. Rev. Lett.*, vol. 85, no. 12, pp. 2633-2636, 2000. DOI: 10.1103/PhysRevLett.85.2633.

[29] G. S. Nusinovich, A. N. Vlasov, and T. M. Antonsen, "Nonstationary Phenomena in Tapered Gyro-Backward-Wave Oscillators," *Phys. Rev. Lett.*, vol. 87, no. 21, 2001. DOI: 10.1103/PhysRevLett.87.218301.

[30] T. Chang, T. Idehara, I. Ogawa, L. Agusu, and S. Kobayashi, "Frequency tunable gyrotron using backward-wave components," *J. Appl. Phys.*, vol. 105, no. 6, p. 063304, 2009. DOI: 10.1063/1.3097334.

[31] S. H. Kao, C. C. Chiu, K. F. Pao, and K. R. Chu, "Competition between harmonic cyclotron maser interactions in the terahertz regime," *Phys. Rev. Lett.*, vol. 107, no. 13, p. 135101, 2011. DOI: 10.1103/PhysRevLett.107.135101.

[32] C. H. Du, and P. K. Liu, "Nonlinear full-wave-interaction analysis of a gyrotron-traveling-wave-tube amplifier based on a lossy dielectric-lined circuit," *Phys. Plasmas*, vol. 17, no. 3, p. 033104, 2010. DOI: 10.1063/1.3339935.

[33] K. R. Chu, H. Y. Chen, C. L. Hung, T. H. Chang, L. R. Barnett, S. H. Chen, T. T. Yang, and D. J. Dialetis, "Theory and experiment of ultrahigh-gain gyrotron traveling wave amplifier," *IEEE Trans. Plasma Sci.*, vol. 27, no. 2, pp. 391-404, 1999. DOI: 10.1109/27.772266.

[34] Q. S. Wang, C. S. Kou, D. B. McDermott, A. T. Lin, K. R. Chu, and N. C. Luhmann, Jr., "High-power harmonic gyro-TWT's. II. Nonlinear theory and design," *IEEE Trans. Plasma Sci.*, vol. 20, no. 3, pp. 163-169, 1992. DOI: 10.1109/27.142816.

[35] N. C. Chen, T. H. Chang, C. P. Yuan, T. Idehara, and I. Ogawa, "Theoretical investigation of a high efficiency and broadband subterahertz gyrotron," *Appl. Phys. Lett.*, vol. 96, no. 16, p. 161501, 2010. DOI: 10.1063/1.3400216.

[36] C. P. Yuan, T. H. Chang, N. C. Chen, and Y. S. Yeh, "Magnetron injection gun for a broadband gyrotron backward-wave oscillator," *IEEE Trans. Plasma Sci.*, vol. 16, no. 7, p. 073109, 2009. DOI: 10.1063/1.3187903.

[37] W. B. Herrmannsfeldt, "EGUN: An electron optics and gun design program," [Online]. Available: http://inspirehep.net/record/265181/files/slac-r-331.pdf